Modeling extended-reaction boundary conditions in time-domain wave-based simulations of room acoustics

Finnur Pind,[1, a)] Cheol-Ho Jeong,[2] Jan S. Hesthaven,[3] Allan P. Engsig-Karup,[4] and Jakob Strømann-Andersen[1]

[1] *Henning Larsen, Copenhagen, Denmark*

[2] *Acoustic Technology Group, Department of Electrical Engineering, Technical University of Denmark, Kongens Lyngby, Denmark*

[3] *Chair of Computational Mathematics and Simulation Science, École polytechnique fédérale de Lausanne, Lausanne, Switzerland*

[4] *Scientific Computing Group, Department of Applied Mathematics and Computer Science, Technical University of Denmark, Kongens Lyngby, Denmark*

This paper presents a general method for modeling extended-reaction surface impedance boundary conditions in time-domain wave-based room acoustic simulations. A sound field separation technique is used to separate the sound field at a boundary into its incident and reflected components, in each time step of the simulation. Once separated, the incidence angle of the incident sound field is determined and the boundary surface impedance is adjusted accordingly. This allows for the incorporation of angle dependent properties of extended-reaction room surfaces in the simulation. The proposed method is validated both analytically and experimentally. An excellent agreement is found between simulations and analytic and measured reference data. Furthermore, a significant improvement in accuracy is observed, when comparing the extended-reaction model to the commonly used local-reaction model, particularly for surface types which exhibit strong extended-reaction behavior. A room with a suspended porous ceiling is simulated using local- and extended-reaction models, where large and perceptually noticeable differences are found, indicating the importance of including extended-reaction behavior in simulations of room acoustics. [a]

Keywords: Room acoustics, wave-based simulations, extended-reaction boundary conditions, sound absorption.

[a] Portions of this work were presented in "Modeling boundary conditions in high-order, nodal, time-domain finite element methods," Proceedings of the 23rd International Congress on Acoustics, Aachen, Germany, September 2019.

[a)] fpin@henninglarsen.com

I. INTRODUCTION

The sound absorption properties of room surfaces have a major influence on the acoustics of rooms. It is therefore important to model these properties accurately when simulating room acoustics. From an acoustical point of view, room surfaces can be divided into two categories, depending on what kind of physical behavior they exhibit when interacting with a sound wave, namely the *local-reaction* (LR) room surfaces and the *extended-reaction* (ER) room surfaces. When a surface exhibits local reaction, the wave is refracted such that it only propagates perpendicularly to the surface, effectively implying that the surface impedance does not vary with the angle of incidence of the incident sound wave.[1] Hence, the frequency dependent normal incidence surface impedance is a sufficient descriptor for a room surface of this type. The local-reaction assumption is generally acceptable for surfaces made of porous materials with a high flow resistivity mounted on a rigid backing.[2] However, in practice, local-reaction surfaces are rather the exception than the rule.[1] There are many commonly used surface types for which the local-reaction assumption has been shown to be inappropriate, particularly surfaces which have elastic properties or fluid layers. This includes porous materials backed by an air cavity, porous materials with low flow resistivity mounted on a rigid backing, and multilayer build-ups of panels, fluids and porous materials.[2–8] For such surface types, waves travel along the boundary surface in a direction parallel to the surface, effectively implying that surface impedance varies with the incidence angle, i.e., they are of the extended-reaction type.[1] Their acoustic properties are thus described by a frequency and angle dependent surface impedance.

Extended-reaction room surfaces and their influence in room acoustic simulations have been studied previously in the literature, primarily in the context of geometrical acoustics simulation methods.[9] Note that it is relatively straightforward to incorporate extended reaction into geometrical methods, such as the image source method[10] or the ray tracing method[11], since in these methods the angle of incidence of an image source or a ray is known and the angle dependent surface impedance can be readily applied. Hodgson and co-authors, using a phased beam-tracing simulation method,[12] demonstrated that large and perceptually noticeable differences in simulated room acoustic parameters are found, depending on whether a local-reaction or an extended-reaction model is used.[5,6] Later, Gunnarsdóttir et al. experimentally validated that for a porous material backed by an air cavity, a pressure based image source method simulation that uses extended reaction shows a substantially better agreement to measurements as compared to using local reaction.[7] Marbjerg et al. developed PARISM[13], a hybrid geometrical simulation tool that takes extended reaction boundary conditions into account and showed that it produced a better agreement to measurements when compared to the ODEON software[14], which relies on random incidence energy based absorption coefficients.[15]

In wave-based room acoustic simulations, the governing partial differential equations (PDEs) that describe wave motion in an enclosure are solved numerically. These methods are in principle very accurate because they inherently account for all wave phenomena such as diffraction, interference and scattering, thus overcoming well known limitations of the geometrical methods.[16,17] Common methods include the finite-difference time-domain method (FDTD),[18] the linear finite element method (h-FEM),[19] the boundary element

method (BEM),[20] the finite volume method (FVM),[21] and, recently, high-order accurate methods such as the spectral element method (SEM),[22] or the discontinuous Galerkin finite element method (DGFEM),[23] due to their cost-efficiency relative to the conventional low-order methods.[24] Room surfaces in wave-based simulation methods, incorporated into the simulation via the boundary conditions, are typically modeled using the normal incidence surface impedance, i.e., assuming local reaction. Modeling extended-reaction surfaces in wave-based simulations has remained a long-standing and largely unsolved problem, rendering the boundary conditions somewhat of an Achilles heel of wave-based simulations. Aretz et al.[2] compared the random incidence (i.e. angle averaged) surface impedance to the normal incidence impedance in FEM simulations and found that in some cases using the random incidence impedance improves accuracy. Tomiku et al.[25] reached a similar conclusion. Aretz et al. also investigated modeling of porous material on a rigid backing using an equivalent homogeneous fluid model, which captures the extended-reaction behavior for this type of surface. Recently, Okuzono et al.[26] presented a method to model the extended-reaction behavior of a single-leaf permeable membrane absorber in FEM simulations. While the methods of Aretz et al. and Okuzono et al. successfully model extended-reaction behavior, they have two notable drawbacks. Firstly, they only apply to a specific room surface type, a porous material mounted on a rigid backing and a single-leaf permeable membrane, respectively. Secondly, they introduce a coupling between the acoustic air domain and the boundary domain, which significantly increases the computational cost of the already computationally expensive wave-based simulation.[2]

This paper presents a general method for modeling the extended-reaction behavior of any room surface, at minimal computational cost. The method is phenomenological in the sense that it does not aim to model the sound propagation inside the surface. Instead, it relies on detecting the local angle of the incident sound field and continuously adjusting the boundary condition according to the incidence angle. To extract the incidence angle, the sound field in front of the boundary is separated into its incident and reflected components using a novel sound field separation technique. Once separated, the incidence angle can be computed from the incident particle velocity.

The paper is organized as follows. Section II presents the governing equations for wave propagation in rooms and their boundary conditions formulation. Section III describes the wave-based scheme and the proposed boundary modeling method. Sections IV and V contain numerical and experimental validation studies of the proposed boundary method. In Sections VI a comparison of a full room simulation, using either local reaction or extended reaction, is presented and, finally, some discussion and concluding remarks are given in Sections VII and VIII.

II. GOVERNING EQUATIONS AND BOUNDARY CONDITIONS

The following set of first order PDEs, subject to the appropriate boundary conditions, describes wave motion in an enclosure,

$$\begin{aligned} \mathbf{v}_t &= -\frac{1}{\rho}\nabla p, \\ p_t &= -\rho c^2 \nabla \cdot \mathbf{v}, \end{aligned} \qquad \text{in } \Omega \times [0, t], \tag{1}$$

where $\mathbf{v}(\mathbf{x}, t)$ is the particle velocity, $p(\mathbf{x}, t)$ is the sound pressure, $\mathbf{x}$ is the position in space of the domain Ω, t is time, c is the speed of sound in air and ρ is the density of the medium ($c = 343\,\mathrm{m/s}$ and $\rho = 1.2\,\mathrm{kg/m^3}$ in this work).

In room acoustics, it is natural to define the boundary conditions in terms of the complex surface impedance $Z(\omega, \theta_i)$, where ω is the angular frequency and θ_i is the incidence angle. For many common room surface types there exist models to estimate the angle and frequency dependent surface impedance. Miki's model is commonly used for porous materials backed by a rigid backing or by an air cavity.[27] Multilayer configurations of panels, fluids and porous materials can be modeled using Biot's theory[28] and a transfer matrix model.[29] There also exist a wide variety of measurement techniques to measure angle and frequency dependent impedance, e.g., using a pressure and particle velocity sensor,[30] microphone arrays,[31] or sound field reconstruction.[32]

The surface impedance relates the pressure $\hat{p}(\omega)$ and the normal particle velocity $\hat{v}_n(\omega)$ at the boundary in the frequency domain as

$$\hat{v}_n(\omega, \theta_i) = \frac{\hat{p}(\omega)}{Z(\omega, \theta_i)}. \tag{2}$$

As mentioned in the introduction, when a room surface is locally reacting, the impedance is independent of the angle θ_i, i.e., $Z(\omega, \theta_i) = Z(\omega)$. The absorption coefficient of a locally reacting room surface, assuming a plane wave impinging on an infinite surface, is thus given by[8]

$$\alpha^l(\omega, \theta_i) = 1 - \left| \frac{Z(\omega, 0) - \rho c / \cos\theta_i}{Z(\omega, 0) + \rho c / \cos\theta_i} \right|^2. \tag{3}$$

Note that even though the surface impedance does not vary with the incidence angle, the absorption coefficient does. However, the $\cos\theta_i$ term is inherently accounted for in Eq. (1).

Conversely, when the surface is of the extended-reaction type, the absorption coefficient is given by

$$\alpha^e(\omega, \theta_i) = 1 - \left| \frac{Z(\omega, \theta_i) - \rho c / \cos\theta_i}{Z(\omega, \theta_i) + \rho c / \cos\theta_i} \right|^2 . \tag{4}$$

III. METHOD

A. Wave-based scheme

In this work, the proposed boundary modeling method is implemented into a SEM wave-based numerical scheme, however, in principle it can be implemented into any time-domain wave-based simulation method without modifications. The SEM scheme is described in detail in Ref.[22] and will thus only be briefly reviewed here. It relies on an arbitrary order piecewise polynomial basis discretization in space and a fourth order implicit-explicit Runge-Kutta discretization in time.[33] This makes the scheme cost-efficient for simulating large scale problems over long simulation times, because the high-order discretization leads to small numerical dispersion and dissipation errors. Furthermore, the scheme supports unstructured meshes, which can contain curvilinear elements, thus making it well suited for simulating complex geometries.

The weak formulation of the governing equations, through the use of the divergence theorem on the pressure equation in Eq. (1), takes the following form

$$\begin{aligned} \int_\Omega \mathbf{v}_t \phi \, \mathrm{d}\Omega &= -\frac{1}{\rho} \int_\Omega \nabla p \, \phi \, \mathrm{d}\Omega, \\ \int_\Omega p_t \phi \, \mathrm{d}\Omega &= -\rho c^2 \left[\int_\Gamma \phi \hat{\mathbf{n}} \cdot \mathbf{v} \, \mathrm{d}\Gamma - \int_\Omega \mathbf{v} \cdot \nabla \phi \, \mathrm{d}\Omega \right], \end{aligned} \tag{5}$$

where Γ denotes the boundary of Ω and ϕ are global basis functions. The boundary conditions are incorporated into the scheme through the boundary integral term in the pressure equation. Inserting a finite dimensional approximation for the unknown variables p and $\mathbf{v}$, yields the following semi-discrete system

$$\begin{aligned} Mv_x' &= -\frac{1}{\rho} S_x p, \quad Mv_y' = -\frac{1}{\rho} S_y p, \quad Mv_z' = -\frac{1}{\rho} S_z p, \\ Mp' &= \rho c^2 \left(S_x^T v_x + S_y^T v_y + S_z^T v_z - v_n B \right), \end{aligned} \tag{6}$$

where v_x, v_y, v_z represent the x, y, z components of the particle velocity, respectively, v_n is the particle velocity at the boundary, to be determined by the boundary modeling method (see Secs. III B and III C), and the sparse global mass and stiffness matrices are

$$\begin{aligned} M_{ij} &= \int_\Omega N_j \; N_i \;\; \mathrm{d}\Omega, \quad S_{x,(ij)} = \int_\Omega (N_j)_x \; N_i \;\; \mathrm{d}\Omega, \\ S_{y,(ij)} &= \int_\Omega (N_j)_y \; N_i \;\; \mathrm{d}\Omega, \quad S_{z,(ij)} = \int_\Omega (N_j)_z \; N_i \;\; \mathrm{d}\Omega, \\ B_{ij} &= \int_\Gamma N_j \; N_i \;\; \mathrm{d}\Gamma, \end{aligned} \tag{7}$$

where the x, y, z subscripts in the integrals denote differentiation and N_i, N_j are global piecewise basis functions.

The spatial domain is divided into N_{el} non-overlapping hexahedral elements and each element is populated with nodes. To support order P basis functions, each element must contain $K_P = (P+1)^3$ nodes. Through a coordinate mapping, each element on the mesh is mapped to a *reference element*, given by

$$\mathcal{I}^3 = \big\{ \mathbf{r} = (r, s, t) | \; -1 \leq (r, s, t) \leq 1 \big\}. \tag{8}$$

In the reference element a set of local, *modal* polynomial basis functions are defined

$$\psi(r,s,t) = \mathcal{P}_i(r)\ \mathcal{P}_j(s)\ \mathcal{P}_k(t), \qquad i,j,k = 0 \ldots P. \tag{9}$$

where $\mathcal{P}_p(z)$ is the p'th order Legendre polynomial. Through a nodal-modal mapping,[34] it is possible to write the local, *nodal* basis functions $\mathcal{N}_i$ on the reference element, without resorting to quadrature rules, by

$$\mathcal{N}_i(\mathbf{r}) = \sum_{n=1}^{P+1} \left(\mathcal{V}^T\right)^{-1}_{i,n}\ \psi_n(\mathbf{r}), \tag{10}$$

where $\mathcal{V}$ is the generalized Vandermonde matrix. From these local basis functions, the global mass and stiffness matrices in Eq. (7) are computed by iterating over the elements and summing the element contributions while relying on the property of domain decomposition, e.g.,

$$M_{ij} = \int_\Omega N_i N_j\, d\Omega = \sum_{n=1}^{N_{el}} \int_{\Omega_n} \mathcal{N}_i^{(n)} \mathcal{N}_j^{(n)}\, d\Omega_n. \tag{11}$$

What remains is to integrate the semi-discrete system in time. The main semi-discrete system is integrated explicitly, whereas the auxiliary differential equations that describe the frequency dependent boundary conditions (see Sec. III B) are integrated implicitly.

B. Modeling local-reaction frequency dependent boundary conditions

To account for the frequency dependency of the impedance in the time-domain simulation, the method of *auxiliary differential equations* is used.[22,35] This section describes how the method is used to account for a local-reaction frequency dependent surface impedance $Z(\omega)$, and in Sec. III C the method is extended to account for extended-reaction boundaries.

The normal incidence boundary admittance $Y = 1/Z$ is mapped to a rational function on the form

$$\begin{aligned} Y(\omega) =& Y_\infty + \sum_{k=1}^{Q} \frac{A_k}{\lambda_k - j\omega} \\ &+ \sum_{k=1}^{S} \left(\frac{B_k + jC_k}{\alpha_k + j\beta_k - j\omega} + \frac{B_k - jC_k}{\alpha_k - j\beta_k - j\omega} \right), \end{aligned} \tag{12}$$

where Y_∞, A_k, B_k, C_k are numerical coefficients, Q is the number of real poles λ_k, and S is the number of complex conjugate pole pairs $\alpha_k \pm j\beta_k$ in the rational function approximation. Using the admittance rather than the impedance is convenient when implementing the governing equations. In this work, vector fitting is used for the rational function approximation.[36] The use of vector fitting for this task is further motivated in Sec. III C.

Inverse Fourier transforming and combining Eqs. (2) and (12) yields

$$\begin{aligned} v_n(t) =& Y_\infty p(t) + \sum_{k=1}^{Q} A_k \phi_k(t) \\ &+ \sum_{k=1}^{S} 2 \left[B_k \psi_k^{(1)}(t) + C_k \psi_k^{(2)}(t) \right], \end{aligned} \tag{13}$$

where ϕ_k, $\psi_k^{(1)}$ and $\psi_k^{(2)}$ are called accumulators. They are determined by a set of ordinary differential equations (ODEs) as

$$\begin{aligned} &\frac{d\phi_k}{dt} + \lambda_k \phi_k(t) = p(t), \\ &\frac{d\psi_k^{(1)}}{dt} + \alpha_k \psi_k^{(1)}(t) + \beta_k \psi_k^{(2)}(t) = p(t), \\ &\frac{d\psi_k^{(2)}}{dt} + \alpha_k \psi_k^{(2)}(t) - \beta_k \psi_k^{(1)}(t) = 0. \end{aligned} \tag{14}$$

These ODEs must be solved in every time step of the simulation along the boundary. Because the ODEs can be stiff, they are solved implicitly to avoid restricting the explicit time stepping method used for the main semi-discrete system in Eq. (6) to an unnecessarily small time

step. The implicit solver is a six stage, fourth order ESDIRK implicit solver, whose Butcher tableau is given in Ref.[33].

C. Modeling extended-reaction frequency dependent boundary conditions

The proposed extended-reaction boundary modeling method works in three steps. First, the sound field at the boundary is separated into its incident and reflected components. Second, the incidence angle θ_i of the incident field is computed. Third, the relevant admittance function $Y(\omega, \theta_i)$ is chosen according to the incidence angle and applied at the boundary. This process is carried out for every boundary node and repeated at every time step of the simulation.

To separate the sound field into its incident and reflected components, a one dimensional (1D) wave-splitting technique is applied.[37] In 1D, the solution of the wave equation consists of a left traveling wave and a right traveling wave. That can also be viewed as an incident wave u_i and a reflected wave u_r, relative to one of the 1D boundaries,

$$u(x,t) = u_i(x - ct) + u_r(x + ct). \tag{15}$$

The unknown variable u can be the pressure field or the particle velocity field. Advection differential operators are defined

$$\delta_1[u] = \frac{\partial u}{\partial t} + c\frac{\partial u}{\partial x}, \qquad \delta_2[u] = \frac{\partial u}{\partial t} - c\frac{\partial u}{\partial x}, \tag{16}$$

and simple inspection reveals

$$\begin{aligned} \delta_1[u_r] &= \delta_1[u], \qquad \delta_1[u_i] = 0, \\ \delta_2[u_i] &= \delta_2[u], \qquad \delta_2[u_r] = 0. \end{aligned} \tag{17}$$

Further algebraic manipulation of Eq. (17) yields

$$\begin{aligned} \frac{\partial u_r}{\partial t} &= \frac{1}{2}\left(\frac{\partial u}{\partial t} + c\frac{\partial u}{\partial x}\right), \\ \frac{\partial u_i}{\partial t} &= \frac{1}{2}\left(\frac{\partial u}{\partial t} - c\frac{\partial u}{\partial x}\right). \end{aligned} \tag{18}$$

These PDEs can be solved numerically, thus allowing for the separation of the incident field and the reflected field from the total field. The right hand side derivatives are replaced with centered second-order finite differences, and the remaining ODEs are solved with a Crank-Nicolson scheme. The finite difference nodes are placed along a 1D line defined by the boundary normal in the three dimensional (3D) space, in front of every boundary node. The field values in the finite difference nodes are computed using interpolation. Figure 1 illustrates the setup. An example of a separated 3D wave is shown in Fig. 2, where a spherical wave impinges on a flat boundary with $\theta_i = 37.6°$ incidence angle at the observation point on the boundary. The boundary condition is frequency independent with a normal incidence absorption coefficient of $\alpha_0 = 0.5$. Note the decreased amplitude of the reflected wave, compared to the incident wave. Furthermore, note the change in sign in the x velocity component.

The sound field separation is applied to the particle velocity x, y, z components. Once the sound field has been separated, the incidence angle is computed with

$$\theta_i = \arccos\left(\frac{\mathbf{v}_i \cdot \hat{\mathbf{n}}}{|\mathbf{v}_i||\hat{\mathbf{n}}|}\right), \tag{19}$$

where $\mathbf{v}_i = [v_{xi}\ v_{yi}\ v_{zi}]^T$ is the incident particle velocity and $\hat{\mathbf{n}}$ is the boundary normal. In this work, the boundary admittance is mapped to rational functions with one degree angular resolution, resulting in a total of 91 admittance functions for a given room surface. Once

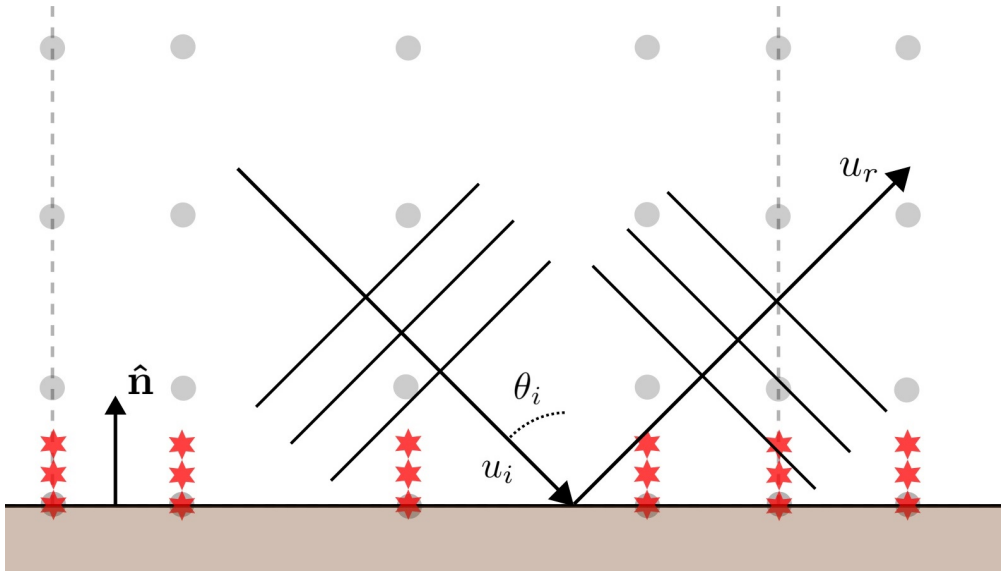

FIG. 1. (Color online) An illustration of the sound field separation setup. The gray dashed lines illustrate the SEM mesh elements and the grey circles are the SEM mesh nodes. The finite difference wave-splitting nodes are placed in front of every boundary SEM node, illustrated as red stars.

the angle of the incident wave is determined, the algorithm selects the admittance function closest to the detected angle.

When doing the rational function approximation for each of the 91 admittance functions, care must be taken to ensure that the distribution of real versus complex conjugate poles in the rational functions is the same for all angles. While this can result in suboptimal curve fitting, meaning that more total poles are required, it ensures that the same ODEs in Eq. (14) are solved in every time step. This is desirable because the solution of the ODEs at time step n requires knowledge of the solution at timestep $n-1$. Thus, the only parameters that change in the simulation, as the incidence angle varies and a new admittance function is chosen, are the Y_∞, A_k, B_k and C_k in Eq. (13). Vector fitting is suitable for this type of

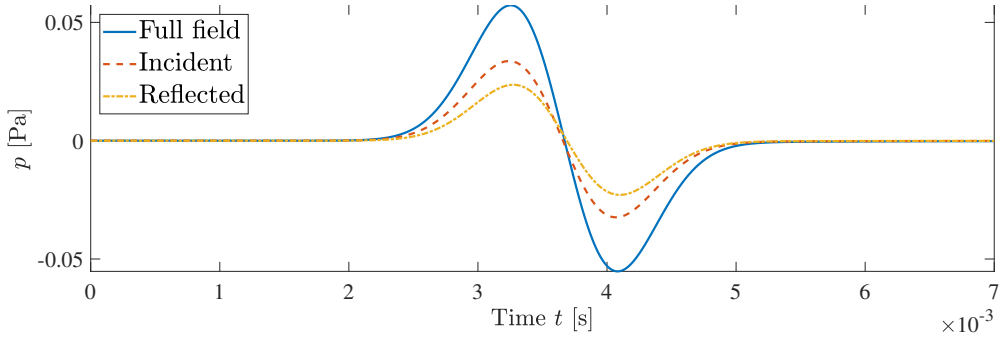

a) Pressure.

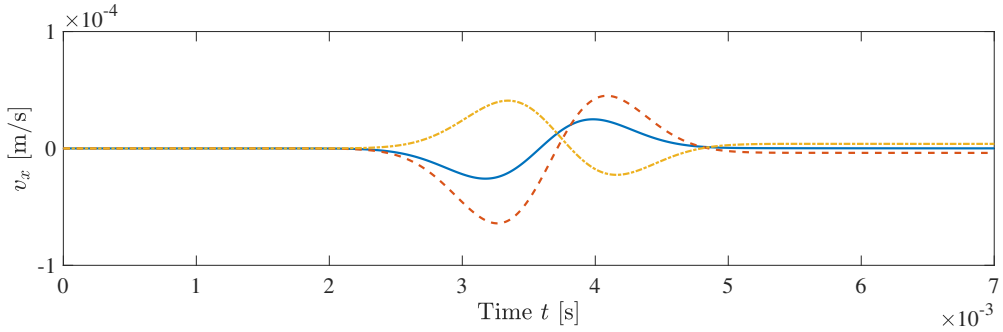

b) x component of particle velocity.

FIG. 2. (Color online) Example of a sound field separation at a boundary of a 3D domain. The domain is a rectangular 3D room $(L_x, L_y, L_z) = (3, 10, 5)$ m. The source is located at $(s_x, s_y, s_z) = (1, 2, 2)$ m and the observation point is located at $(r_x, r_y, r_z) = (0, 2.577, 2.5)$ m. The angle between the source and the observation point is $\theta_i = 37.6°$and the boundary condition is frequency independent with a normal incidence absorption coefficient of $\alpha_0 = 0.5$.

function approximation, as the real versus complex pole distribution can be kept consistent across all incidence angles.[36]

IV. ANGLE DETECTION ACCURACY ANALYSIS

Since the sound field separation is computed along a 1D line, defined by the boundary normal in 3D space, the accuracy of the proposed separation method will vary with the

incidence angle. When a wave is traveling close to normal incidence, the energy flow is more or less along the boundary normal and hence high accuracy in the separation and angle computation should be expected. However, as the incidence angle approaches grazing incidence, the energy flow is only partially along the boundary normal, and a decrease in accuracy should be expected. A two dimensional (2D) test case, using a plane wave incidence, is considered to analyze the angle detection accuracy as a function of the incidence angle. A rectangular domain is used, where the left-right boundaries are made to be periodic. The bottom boundary is the boundary of interest, where the sound field separation and angle detection is performed. The top boundary is an absorbing layer. The width of the domain is adjusted according to the incidence angle to ensure periodicity. The plane wave incidence is produced using a scattered field formulation.[38] The 2D incident plane wave solution is

$$\begin{aligned} p_i &= \exp(j(\mathbf{kx} - \omega t)), \\ \mathbf{v}_i &= \frac{1}{\rho c}\hat{\mathbf{k}} \exp(j(\mathbf{kx} - \omega t)), \end{aligned} \tag{20}$$

where $\mathbf{k} = k\hat{\mathbf{k}} = k[\cos\theta_i \ \sin\theta_i]^T$ is the wave vector. In the scattered field formulation, the total field solution of Eq. (1) is defined as a superposition of the incident field and the scattered field

$$\mathbf{v} = \mathbf{v}_i + \mathbf{v}_s, \qquad p = p_i + p_s. \tag{21}$$

Inserting this into Eq. (1) yields

$$\begin{aligned} (\mathbf{v_s})_t &= -\frac{1}{\rho}\nabla p_s - \gamma(y)\mathbf{v_s}, \\ (p_s)_t &= -\rho c^2 \nabla \cdot \mathbf{v_s} - \gamma(y) p_s, \end{aligned} \tag{22}$$

since $(\mathbf{v}_i, p_i)$ satisfies Eq. (1). This system is solved using the wave-based scheme with $(\mathbf{v}_s, p_s) = 0$ at $t = 0$ and with a frequency independent boundary condition at the bottom

boundary, which induces the scattered field reflection

$$\hat{\mathbf{n}} \cdot \mathbf{v}_s = \frac{p_i + p_s}{Z} - \hat{\mathbf{n}} \cdot \mathbf{v}_i. \tag{23}$$

The terms with the γ function in Eq. (22) are added to implement the absorbing layer at the top boundary by using

$$\gamma(y) = \begin{cases} 0 & y \leq L_y - a, \\ \frac{(y-(L_y-a))^q}{\Delta t} & L_y - a \leq y \leq L_y, \end{cases} \tag{24}$$

where a is the width of the absorbing layer, q is a numerical parameter that dictates how rapidly the wave decays as it enters the absorbing layer, and L_y is the length of the domain in the y dimension. The parameters a and q must be tuned to ensure sufficient absorption at the top boundary. In this work, setting $q = 4$ and following a common rule of thumb of having the layer width be at least two wavelengths,[39] yields satisfactory performance of the absorbing layer.

The sound field separation and subsequent angle detection accuracy are tested for three boundary conditions, by having frequency independent normal incidence absorption coefficients of $\alpha_0 = 0.1, 0.5, 0.9$. The results can be seen in Fig. 3. The angle detection error is defined as $|\overline{\theta_e} - \theta_i|$, where $\overline{\theta_e}$ is the time averaged estimated angle and θ_i is the true incidence angle of the plane wave. As expected, the angle detection error is very low for all tested boundary conditions for small incidence angles, at less than 5° for incidence angles smaller than or equal to 30°. As the incidence angle increases, the error also increases, however, for all cases it is less than 15°. The error is larger for less absorbing surfaces, because here the

reflected field is more prominent. For the highly absorptive case, the error is less than 5° for incidence angles up to 70°.

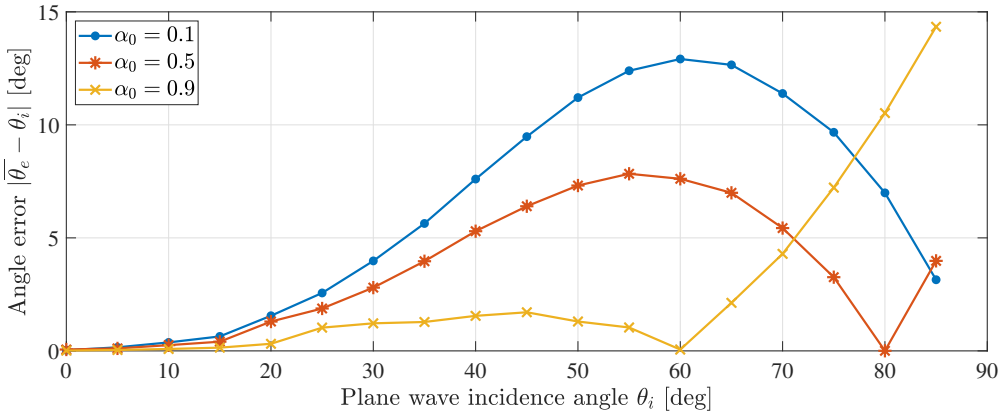

FIG. 3. (Color online) Accuracy of the proposed sound field separation and subsequent angle detection procedure for a plane wave incidence.

V. SINGLE REFLECTION VALIDATION STUDY

A. Study setup

In this validation study, the transfer function (TF) between a source and a receiver in the presence of a single flat reflecting surface is investigated. Simulated transfer functions are compared against an analytic solution[40] and against measurements done in an anechoic chamber. The position of the receiver is varied to test a wide range of different incidence angles, ranging from $\theta_i = 12°$ to $\theta_i = 70°$. Figure 4 shows the setup of the validation study and an image from the measurements in the anechoic chamber. In the simulation, a large $4 \times 8 \times 4$ m rectangular room is used and all parasitic reflections from other surfaces are eliminated from the simulated impulse response, to ensure that only the direct sound

and a single reflection from the surface of interest is included in the response. Table I details the source and receiver positions used. A $P = 4$ basis function order and a very high spatio-temporal resolution is used in the simulation, with roughly 23 points in space per wavelength at 600 Hz, the highest frequency of interest. This ensures that numerical dispersion and dissipation errors are negligible.

ID	Position	Incidence angle θ_i
Source	$(0.75, 2.32, 2.00)$	-
R1	$(0.75, 2.64, 2.00)$	12°
R2	$(1.20, 4.27, 2.00)$	45°
R3	$(1.20, 4.64, 2.00)$	50°
R4	$(0.75, 4.46, 2.00)$	55°
R5	$(0.75, 4.72, 2.00)$	58°
R6	$(0.75, 4.92, 2.00)$	60°
R7	$(0.40, 4.79, 2.00)$	65°
R8	$(0.20, 4.67, 2.00)$	68°
R9	$(0.20, 4.93, 2.00)$	70°

TABLE I. Source and receiver positions used in the single reflection validation study.

Two room surface types are considered; 1) a 5 cm thick porous material mounted on a rigid backing and 2) the same 5 cm thick porous material backed by a 15 cm thick air cavity.

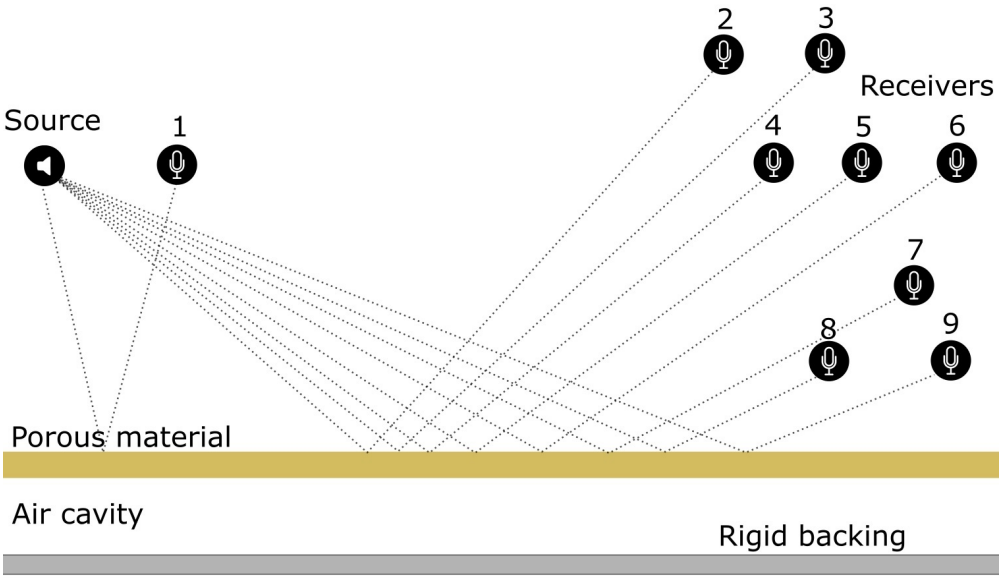

a) Setup schematic.

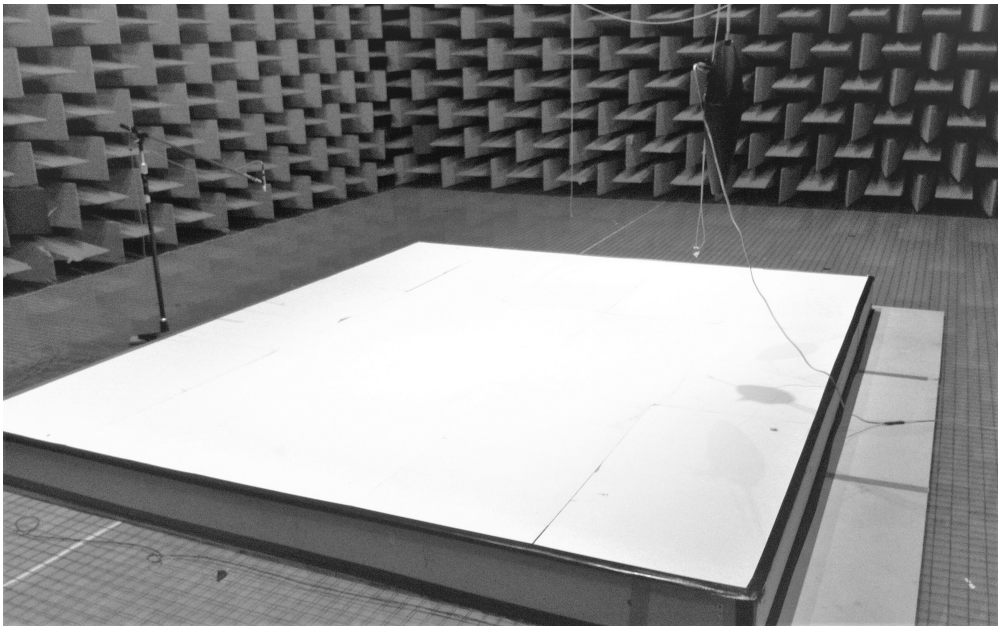

b) Image from the measurements.

FIG. 4. (Color online) Single reflection validation study setup.

The porous material has a flow resistivity of $\sigma_{\text{mat}} = 14\,400\,\text{Ns/m}^4$. The frequency and angle dependent impedance for these surfaces are estimated using Miki's model.[27] Figure 5 shows the frequency and angle dependent absorption coefficient of the rigid backing case, computed

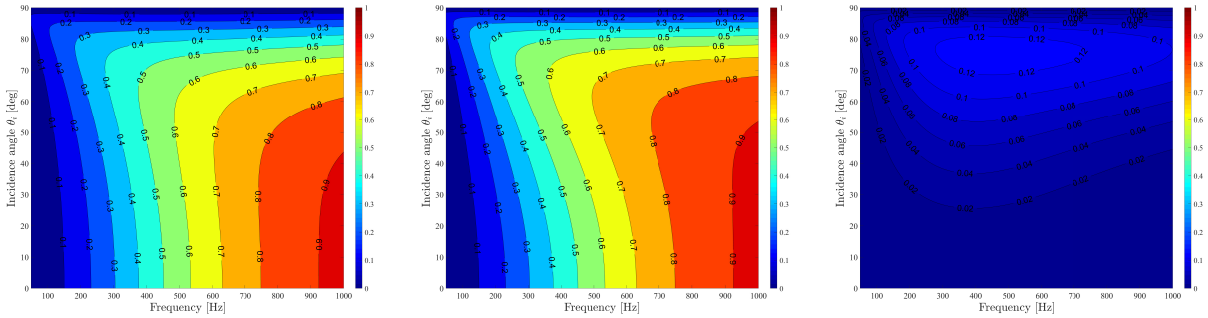

a) Local reaction. b) Extended reaction. c) Difference.

FIG. 5. (Color online) Frequency and angle dependent absorption coefficient of the 5 cm thick porous material mounted on a rigid backing. The impedance is estimated using Miki's model.

using either the local-reaction assumption, Eq. (3), or the extended-reaction assumption, Eq. (4). Figure 6 shows the same for the air cavity case. For the rigid backing case, there are relatively small differences between the results of the local-reaction assumption and the extended-reaction assumption. The biggest difference is seen close to grazing incidence, with a maximum magnitude difference of around 0.13 in the absorption coefficient. However, for the air cavity case, considerable differences are found between the results of the local-reaction assumption and the extended-reaction assumption. The differences become apparent for incidence angles as small as 30° and for some angles and frequencies the difference magnitude is upwards of 0.4 in the absorption coefficient.

The admittance functions given by Miki's model must be mapped to rational functions in order for them to be incorporated into the simulation. As described in Sec. III C, the admittance functions are mapped with 1° angular resolution, resulting in a total of 91 functions per surface type. 14 poles are used in the function approximation. This gives a good approximation of the admittance functions. Table II shows the relative errors of the

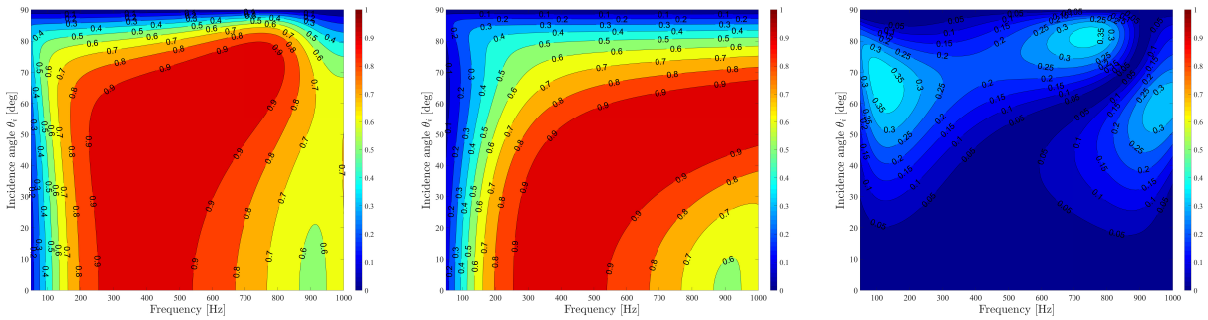

a) Local reaction. b) Extended reaction. c) Difference.

FIG. 6. (Color online) Frequency and angle dependent absorption coefficient of the 5 cm thick porous material backed by a 15 cm thick air cavity. The impedance is estimated using Miki's model.

function approximation. The relative error for a given angle is computed by

$$\epsilon(\theta_i) = \frac{\overline{|Y(\omega,\theta_i) - Y_{\text{fit}}(\omega,\theta_i)|}}{\overline{Y}(\omega,\theta_i)}, \tag{25}$$

where $\overline{Y}$ indicates the mean across frequency. The table lists the error for the normal incidence admittance $\epsilon(0)$, the mean error across all angles $\overline{\epsilon}(\theta_i)$, the maximum error $\max \epsilon(\theta_i)$, and the standard deviation $\sigma(\epsilon)$.

The measurements are carried out in a large anechoic chamber of around $1000\,\text{m}^3$. The chamber has a lower limiting frequency of approximately 50 Hz. The rigid backing is realized by a 3 cm thick wooden panel which is placed on the mesh floor. The size of the absorbing sample is $10.8\,\text{m}^2$, with dimensions $3 \times 3.6\,\text{m}$. The air cavity mounting is a type E mounting configuration according to ISO 354.[41] The flow resistivity of the porous material sample is measured in an impedance tube following the method suggested by Ren et al.[42] and found to be $\sigma_{\text{mat}} = 14\,400\,\text{Ns/m}^4$. An omni-directional sound source of type B&K 4295 and a $\frac{1}{2}$ inch microphone of type B&K 4192 is used (Bruel & Kjaer, Naerum, Denmark). The source

Material	$\epsilon(0)$	$\overline{\epsilon}(\theta_i)$	$\max \epsilon(\theta_i)$	$\sigma(\epsilon)$
Rigid backing real	0.009%	0.011%	0.013%	0.001%
Rigid backing imag.	0.016%	0.020%	0.025%	0.003%
Air cavity real	0.440%	0.296%	0.474%	0.098%
Air cavity imag.	1.031%	0.765%	1.273%	0.252%

TABLE II. Relative error in the rational function approximation for the two surface types considered in the single reflection validation test.

signal is an exponential sine sweep. For the measurment, a two-step procedure suggested by Suh et al. is used.[43] A transfer function TF_c between the source and receiver is first measured without the presence of the absorbing sample, with a source to receiver distance of r_c. Then, a transfer function TF_s with the absorbing sample is measured. The final measured transfer function is given as

$$TF_m(f) = \frac{\rho}{4\pi} \frac{e^{-jkr_c}}{r_c} \frac{TF_s}{TF_c}. \tag{26}$$

B. Results

The results are analyzed in the frequency range of 150 to 600 Hz. In this range, the influence of uncertainty is reduced, e.g., it falls within the valid frequency range of the impedance tube flow resistivity measurement. Furthermore, 150 Hz is far above the lower limiting frequency of Miki's model, which is roughly $f_l = 0.001\sigma_{\text{mat}} = 14$ Hz in this case[44]

316 and it is also above the lower limiting frequency of the sound source and the anechoic
317 chamber used in the measurement.

318 Figure 7 shows transfer functions for selected incidence angles for the rigid backing case.
319 The figure reveals that there are only small differences between using the LR method and
320 the ER method for this surface type. When comparing against the analytic solution, the ER
321 method shows an excellent agreement. The LR model shows good agreement as well, with
322 only some small differences visible, particularly for higher incidence angles. Figure 8a shows
323 the mean error between the simulation and the analytic solution for all considered incidence
324 angles. The mean error is defined as the absolute difference between the normalized reference
325 and simulated transfer functions averaged over the frequency range (in dB). Figure 8b shows
326 a spectral shape similarity measure S, inspired by the modal assurance criterion (MAC),
327 defined by

$$S = \frac{|TF_{\text{ref}}^T TF_{\text{sim}}|^2}{(TF_{\text{ref}}^T TF_{\text{ref}})(TF_{\text{sim}}^T TF_{\text{sim}})}, \tag{27}$$

328 where TF_{ref} is the reference transfer function (measured or analytic) and TF_{sim} is the
329 simulated transfer function. Clearly, the error is very low for this rigid backing case when
330 comparing against the analytic solution. The ER method begins to slightly outperform the
331 LR method for incidence angles larger than 60°. This is in good agreement with the material
332 properties shown in Fig. 5. The spectral shape similarity is essentially equal to unity for all
333 incidence angles considered, for both the LR and the ER method.

334 Figure 9 contains the same error measures, but now comparing against the measurement
335 results instead of the analytic solution. Naturally, there are more fluctuations in the mea-
336 sured transfer function as compared to the analytic solution. This yields somewhat higher

errors, but nevertheless a good agreement is found between measurement and simulations. As before, the LR method and the ER method perform equally well up to incidence angles around 60°, after which the ER method slightly outperforms the LR method. Virtually no difference in spectral shape similarity is seen between the results of the LR method or the ER method.

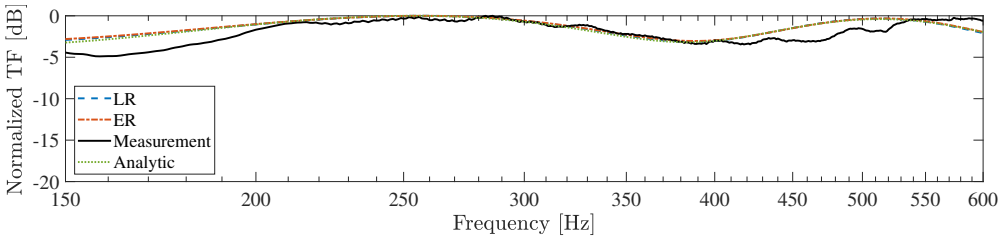

a) $\theta_i = 12°$.

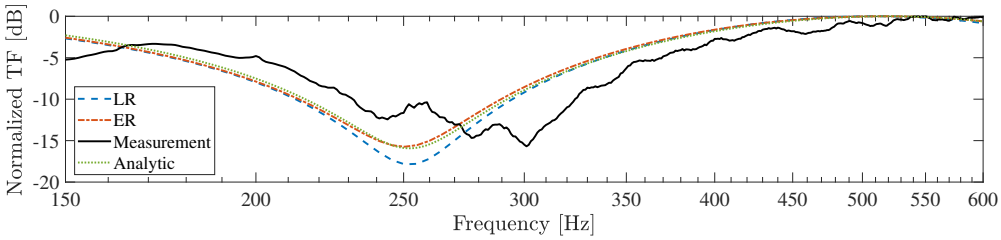

b) $\theta_i = 55°$.

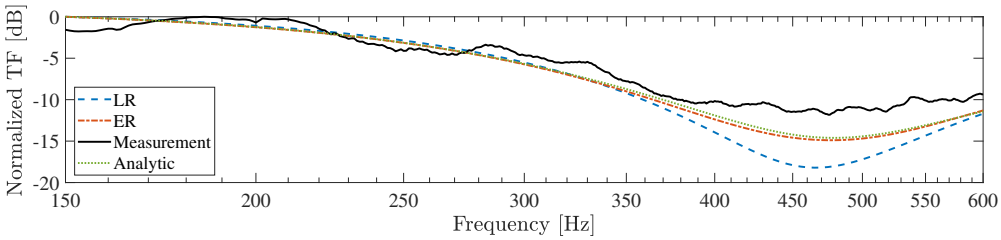

c) $\theta_i = 68°$.

FIG. 7. (Color online) Transfer functions for selected incidence angles, for the rigid backing case.

Figure 10 shows transfer functions for selected incidence angles for the air cavity case. For the higher incidence angles, large differences between the results of the LR method or the ER method for the boundary are now clear. This is as expected, since this surface

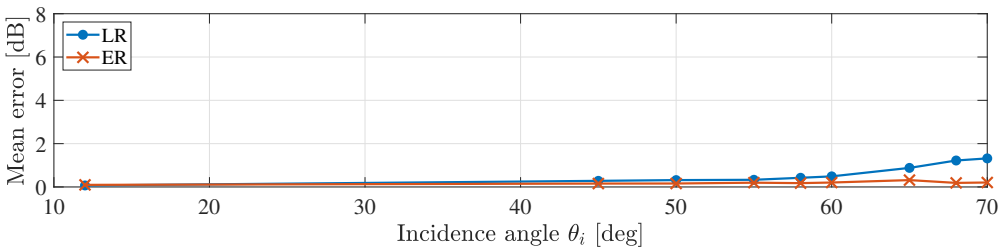

a) Mean error.

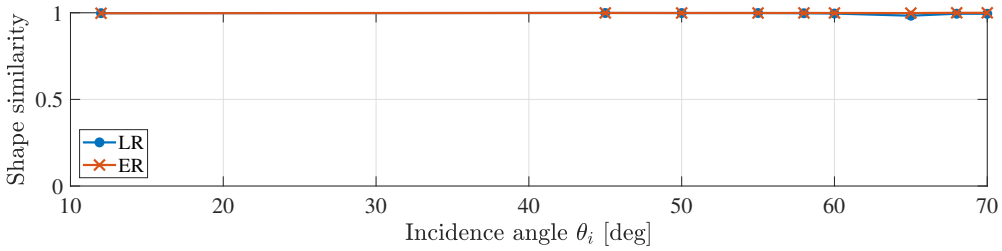

b) Spectral shape similarity.

FIG. 8. (Color online) Error measures for the rigid backing case when comparing against the analytic solution.

is known to have strong extended-reaction behavior, as shown in Fig. 6. Clearly, the ER method matches both the measured and analytically calculated reference transfer functions significantly better than the LR method. The mean error and the spectral shape similarity for all considered incidence angles, when comparing simulations against the analytic solution, are shown in Fig. 11. Already at 45° incidence angle, the error for the LR method is larger than for the ER method. As the incidence angle increases, the ER method begins to significantly outperform the LR method, as the error for the LR method increases rapidly with incidence angle, whereas it only increases slightly for the ER method. At 70°, the highest incidence angle tested, the mean error for the LR method is 6.9 dB, but only 2.2 dB for the ER method. When looking at the spectral shape similarity, the ER method retains the spectral shape nearly perfectly, whereas for the LR method the similarity drops sharply

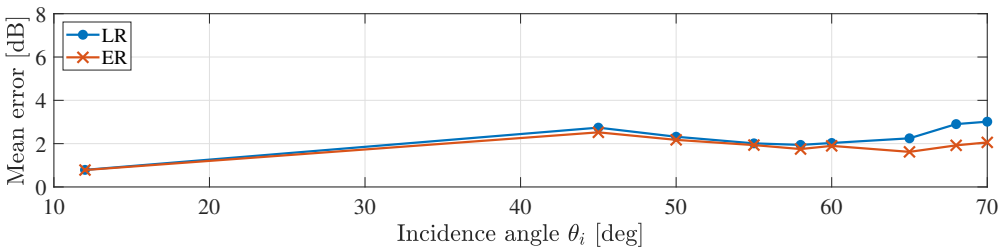

a) Mean error.

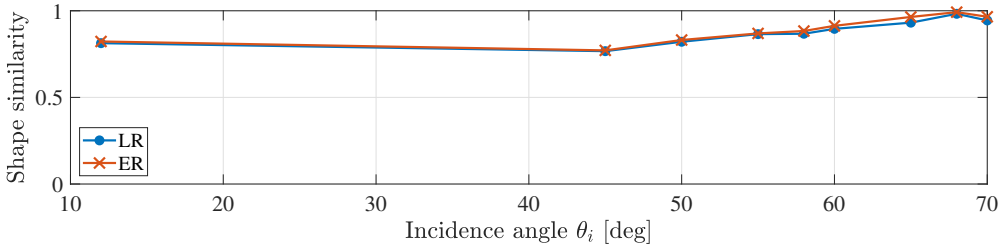

b) Spectral shape similarity.

FIG. 9. (Color online) Error measures for the rigid backing case when comparing against the measurement.

for incidence angles above 50°. Figure 12 shows the error measures when comparing against measurements. The same trend is seen here, with lower errors and higher shape similarity when using the ER method, particularly for the larger incidence angles.

VI. ROOM RESPONSE NUMERICAL EXPERIMENT

To give insight into how large a difference in a simulated room impulse response can be expected, with different boundary modeling methods, a numerical experiment is carried out where the impulse response of a small 3D rectangular room of size $1 \times 5 \times 1$ m is simulated. A disproportionate room shape is chosen to induce grazing incidence waves. The surface impedance of the ceiling is modeled with Miki's model as a 5 cm porous material of flow resistivity $\sigma_{\text{mat}} = 14\,400\,\text{Ns/m}^4$ backed by a 15 cm air cavity, i.e., the same room

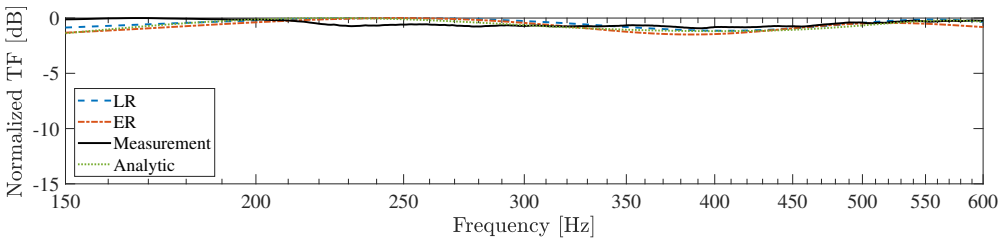

a) $\theta_i = 12°$.

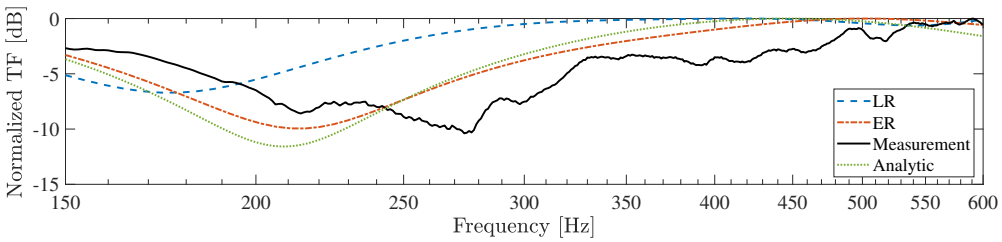

b) $\theta_i = 55°$.

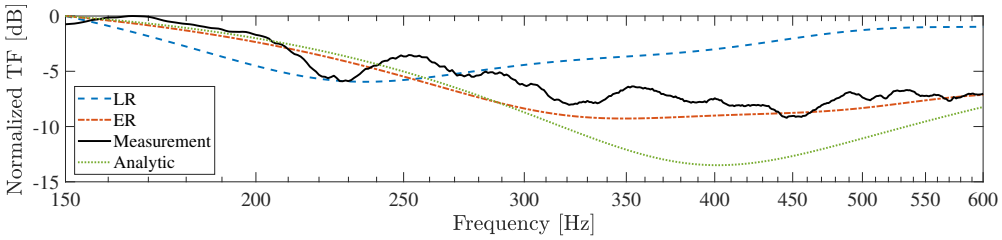

c) $\theta_i = 68°$.

FIG. 10. (Color online) Transfer functions for selected incidence angles, for the air cavity case.

surface configuration used in the single reflection validation study, whose sound absorption properties are shown in Fig. 6. This surface is modeled using either the LR boundary method or the ER boundary method. All other surfaces are perfectly rigid. The impulse response is simulated for two receiver positions, namely $R_1 = (0.70, 4.50, 0.90)$ m and $R_2 = (0.8, 3.00, 0.45)$ m. The source is located at $S = (0.30, 0.50, 0.90)$ m. A $P = 4$ basis function and a high spatio-temporal resolution is used, with 20 points per wavelength at 700 Hz, the highest frequency of interest. The simulation time is 0.5 second and the initial condition is a Gaussian pulse with spatial width $\sigma = 0.2\,\mathrm{m}^2$.

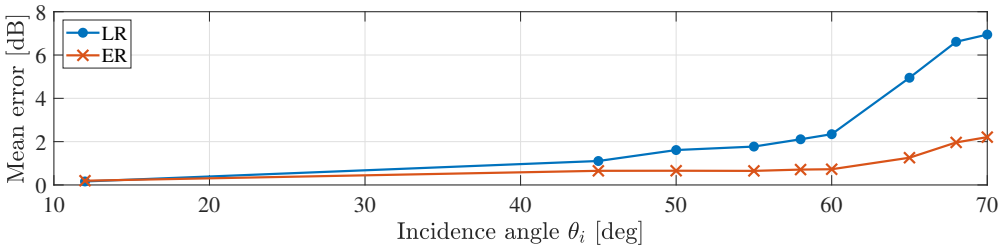

a) Mean error.

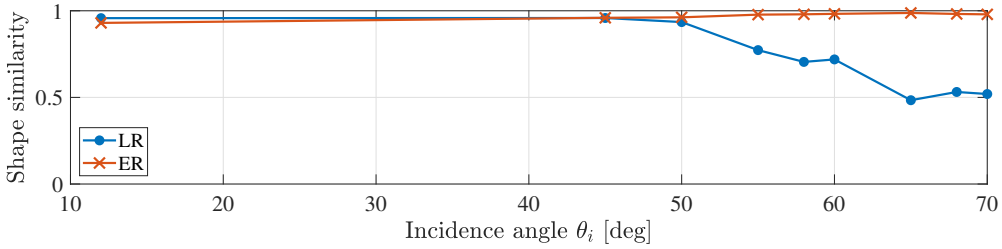

b) Spectral shape similarity.

FIG. 11. (Color online) Error measures for the air cavity case when comparing against the analytic solution.

Figure 13 shows the simulated frequency responses for R_1, obtained by Fourier transforming the simulated impulse responses. The responses are shown both in narrowband form and in 1/3 octave bands. Notable differences are seen between the two responses, as large as 4.0 dB and a mean difference of 2.3 dB, for the 1/3 octave band values. The frequency responses for R_2 are shown in Fig. 14. Again notable differences are seen, with the largest difference being 4.8 dB and the mean difference being 1.4 dB, for the 1/3 octave band values. R_1 is positioned close to the absorbing surface in order to promote grazing incidence waves from the source, whereas R_2 is close to the middle of the room. It therefore is expected that a larger mean difference between LR and ER is seen for R_1.

Tables III and IV show the simulated T_{20} reverberation time, derived from the simulated impulse responses, for R_1 and R_2, respectively. The differences between the two boundary

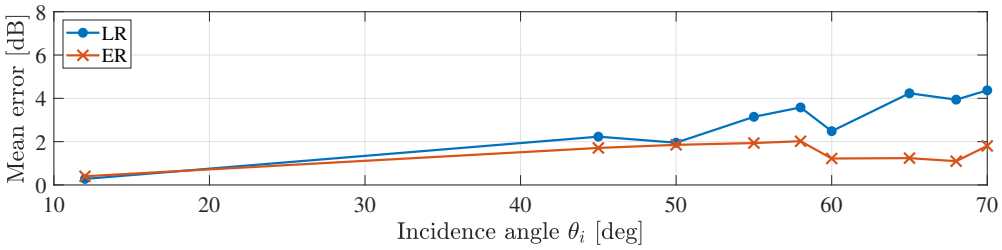

a) Mean error.

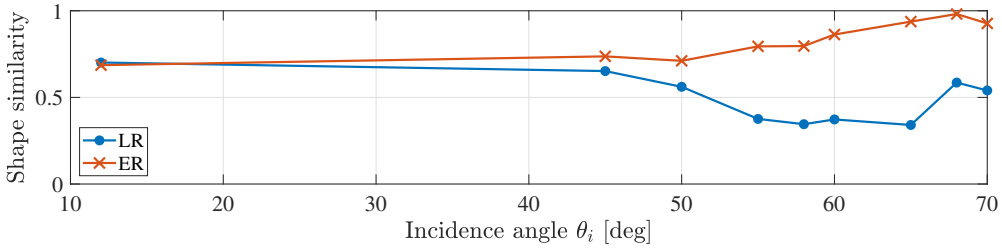

b) Spectral shape similarity.

FIG. 12. (Color online) Error measures for the air cavity case when comparing against the measurement.

modeling approaches are even more evident by looking at the reverberation time than the frequency response. The just-noticeable-difference (JND) of reverberation time is generally taken to be 5%.[45] The difference in reverberation time is found to be several JNDs, ranging from roughly 5 to 11 JNDs for different octave bands. It is clear that for this room, the difference between using the LR model and the ER model would be perceptually noticeable. We argue that the simulated response using the ER method will be the more accurate one, as the method has been shown in Sec. V to better model sound reflection from room surfaces, particularly for surfaces that have strong extended-reaction behavior.

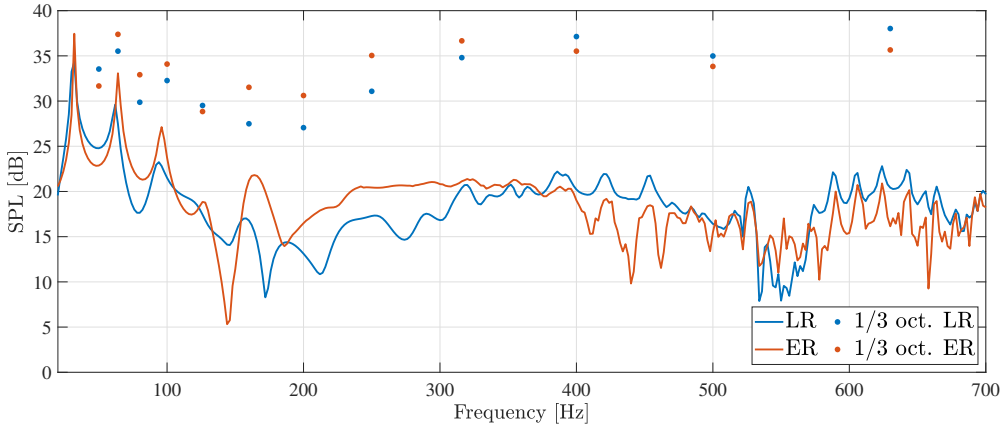

FIG. 13. (Color online) Frequency response of a $1 \times 5 \times 1$ m room, for $R_1 = (0.70, 4.50, 0.90)$ m and $S = (0.30, 0.50, 0.90)$ m. The ceiling is a 5 cm porous material mounted with a 15 cm air cavity and is modeled using either the LR boundary method or the proposed ER boundary method. All other surfaces are rigid.

Octave band	LR T_{20}	ER T_{20}	Difference
63 Hz	0.61 s	0.99 s	−38.3% (7.7 JND)
125 Hz	0.26 s	0.50 s	−48.0% (9.6 JND)
250 Hz	0.19 s	0.13 s	+46.2% (9.2 JND)
500 Hz	0.45 s	1.05 s	−57.1% (11.4 JND)

TABLE III. Simulated reverberation time for R_1.

VII. DISCUSSION

The proposed boundary method has been shown to significantly improve the accuracy of modeling the sound absorption properties of room surfaces, particularly of room surfaces that

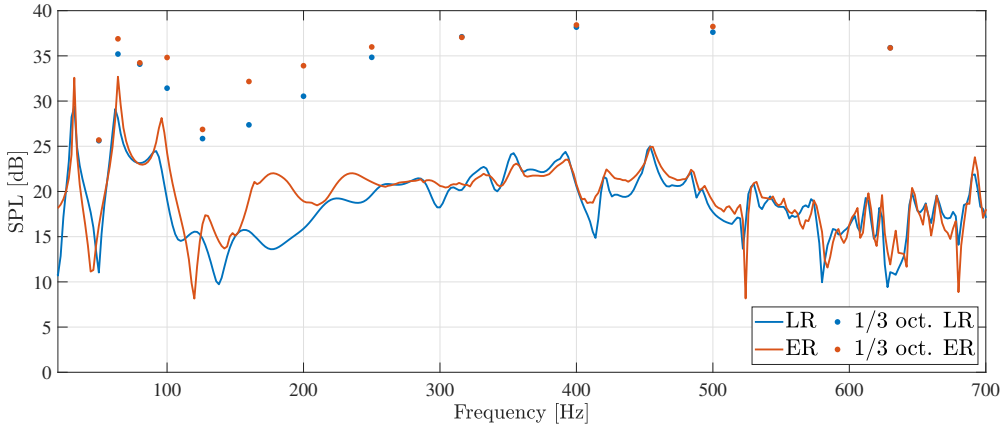

FIG. 14. (Color online) Frequency response of a $1 \times 5 \times 1$ m room, for $R_2 = (0.8, 3.00, 0.45)$ m and $S = (0.30, 0.50, 0.90)$ m. The ceiling is a 5 cm porous material mounted with a 15 cm air cavity and is modeled using either the LR boundary method or the proposed ER boundary method. All other surfaces are rigid.

Octave band	LR T_{20}	ER T_{20}	Difference
63 Hz	0.61 s	0.99 s	−38.3% (7.7 JND)
125 Hz	0.27 s	0.50 s	−46.0% (9.2 JND)
250 Hz	0.19 s	0.14 s	+46.2% (9.2 JND)
500 Hz	0.41 s	0.56 s	−26.8% (5.4 JND)

TABLE IV. Simulated reverberation time for R_2.

exhibit prominent extended-reaction behavior. Indeed, the method captures the reflection from a porous material backed by an air cavity—a room surface configuration known to exhibit strong extended reaction—with high precision for all tested incidence angles, see, e.g., Figs. 11 and 12.

401 The accuracy of the proposed boundary method depends on how well the incidence angle
402 of the incident sound field can be determined. As shown in Fig. 3, the accuracy of the
403 method is higher when the room surface is highly absorbing. Many common room surfaces
404 that exhibit extended-reaction behavior are indeed highly absorbing, e.g., porous materials
405 backed by an air cavity. It could be interesting as future work to investigate the performance
406 of the proposed method on modeling, e.g., vibrating airtight panels, which are also known
407 to exhibit extended-reaction behavior but are less absorbing.

408 The impact of modeling surfaces either as extended-reaction or local-reaction will nat-
409 urally be highly case dependent, e.g., depending on room surface types, room geometry,
410 source and receiver positions etc. For the test case presented in Sec. VI, large and percep-
411 tually noticeable differences are found. For a more thorough investigation of the importance of
412 modeling extended-reaction boundaries, the reader is pointed to, e.g., Ref.[5]. The ultimate
413 validation of the proposed method would be subjective tests. This remains for future work.

414 When comparing simulations against measurements, there are always uncertainties in-
415 volved. While steps have been taken to minimize the uncertainties, there are some noticeable
416 fluctuations in the measured transfer functions that are likely caused by edge diffraction ef-
417 fects, due to the finite sample size. Other sources of uncertainty are, e.g., sound source
418 imperfections, material mounting and material uniformity. However, the measurements do
419 confirm the general trend and the improved accuracy of the ER method. It could be valu-
420 able to carry out uncertainty quantification on both the measurement and the simulation, to
421 analyze how sensitive the data is to changes in input parameters and measurement settings.

When a sound field becomes very diffuse, and a surface is hit simultaneously with many different waves coming in from many different angles, the proposed method will detect the most prominent wave component and adjust the boundary condition according to that incidence angle. Perhaps it is sufficient to use a random incidence surface impedance for the later parts of an impulse response, when the reflection density becomes very high, and restrict the proposed ER method to modeling the perceptually important early reflections. This is a task for future work.

The proposed method is found to add very little additional computational cost to the simulations. In all cases, the added computation time is found to be less than 10%, using the non-optimized sequential implementation used in this work. A benefit of the proposed method is that it is entirely local in its implementation and there is no interaction between boundary nodes. This locality could be exploited in parallelization of the method implementation, resulting in even less added computation time.

VIII. CONCLUSION

A general method for modeling extended-reaction boundary conditions has been presented. The method relies on a novel sound field separation technique, which separates the sound field in front of a boundary into its incident and reflected components. The incidence angle of the incident sound field is then determined from the local particle velocity and then the boundary conditions are adjusted according to the incidence angle. This allows the simulation to incorporate the angle dependent properties of extended-reaction boundaries.

The accuracy of the method is validated both analytically and experimentally. For all cases an improvement in accuracy is seen when using the extended-reaction modeling method, as compared to the local-reaction modeling method. The accuracy improvement is particularly large for surfaces which exhibit strong ER behavior and particularly for high incidence angles. For these cases, using the LR method results in large errors, whereas the ER method models the boundary properties with higher accuracy.

ACKNOWLEDGMENTS

This research has been partially funded by the Innovation foundation and the Realdania foundation in Denmark. The infrastructure at the Technical University of Denmark Computing Center has been used for running simulations. Finally, the authors wish to thank Bjørn Gustavsen at SINTEF for sharing his insights regarding vector fitting.

REFERENCES

[1]H. Kuttruff. *Room Acoustics*. Taylor & Francis, 5th edition, 2009. Ch. 2.

[2]M. Aretz and M. Vorlander. Efficient modelling of absorbing boundaries in room acoustic FE simulations. *Acta Acust. Acust.*, 96(6):1042–1050, 2010.

[3]E. A. G. Shaw. The acoustic wave guide. II. Some specific normal acoustic impedance measurements of typical porous surfaces with respect to normally and obliquely incident waves. *J. Acoust. Soc. Am.*, 25(2):231–235, 1953.

460 [4]C. Klein and A. Cops. Angle dependence of the impedance of a porous layer. *Acustica*,
461 44:258–264, 1980.

462 [5]M. Hodgson and A. Wareing. Comparisons of predicted steady-state levels in rooms with
463 extended- and local-reaction bounding surfaces. *J. Sound Vib.*, 309(1):167–177, 2008.

464 [6]B. Yousefzadeh and M. Hodgson. Energy- and wave-based beam-tracing prediction of
465 room-acoustical parameters using different boundary conditions. *J. Acoust. Soc. Am.*,
466 132(3):1450–1461, 2012.

467 [7]K. Gunnarsdóttir, C.-H. Jeong, and G. Marbjerg. Acoustic behavior of porous ceiling
468 absorbers based on local and extended reaction. *J. Acoust. Soc. Am.*, 137(1):509–512,
469 2015.

470 [8]C.-H. Jeong. Guideline for adopting the local reaction assumption for porous absorbers
471 in terms of random incidence absorption coefficients. *Acta Acust. Acust.*, 97(5):779–790,
472 2011.

473 [9]L. Savioja and U. P. Svensson. Overview of geometrical room acoustic modeling techniques.
474 *J. Acoust. Soc. Am.*, 138(2):708–730, 2015.

475 [10]J. B. Allen and D. A. Berkley. Image method for efficiently simulating small-room acous-
476 tics. *J. Acoust. Soc. Am.*, 65:943–950, 1979.

477 [11]A. Krokstad, S. Strom, and S. Soersdal. Calculating the acoustical room response by the
478 use of a ray tracing technique. *J. Sound Vib.*, 8(1):118–125, 1968.

479 [12]A. Wareing and M. Hodgson. Beam-tracing model for predicting sound fields in rooms
480 with multilayer bounding surfaces. *J. Acoust. Soc. Am.*, 118(4):2321–2331, 2005.

[13]G. Marbjerg, J. Brunskog, C.-H. Jeong, and E. Nilsson. Development and validation of a combined phased acoustical radiosity and image source model for predicting sound fields in rooms. *J. Acoust. Soc. Am.*, 138(3):1457–1468, 2015.

[14]G.M. Naylor. ODEON—Another hybrid room acoustical model. *Appl. Acoust*, 38(2-4):131–143, 1993.

[15]G. Marbjerg, J. Brunskog, and C.-H. Jeong. The difficulties of simulating the acoustics of an empty rectangular room with an absorbing ceiling. *Appl. Acoust.*, 141:35–45, 2018.

[16]Y. W. Lam. Issues for computer modelling of room acoustics in non-concert hall settings. *Acoust. Sci. Tech.*, 26(2):145–155, 2005.

[17]F. Brinkmann, L. Aspock, D. Ackermann, S. Lepa, M. Vorlander, and S. Weinzierl. A round robin on room acoustical simulation and auralization. *J. Acoust. Soc. Am.*, 145(4):2746–2760, 2019.

[18]D. Botteldooren. Finite-difference time-domain simulation of low-frequency room acoustic problems. *J. Acoust. Soc. Am.*, 98(6):3302–3308, 1995.

[19]A. Craggs. A finite element method for free vibration of air in ducts and rooms with absorbing walls. *J. Sound Vib.*, 173:568–576, 1994.

[20]J. A. Hargreaves, L. R. Rendell, and Y. W. Lam. A framework for auralization of boundary element method simulations including source and receiver directivity. *J.Acoust. Soc. Am.*, 145(4):2625–2637, 2019.

[21]S. Bilbao. Modeling of complex geometries and boundary conditions in finite difference/finite volume time domain room acoustics simulation. *IEEE Trans. Audio, Speech,*

Lang. Proc., 21(7):1524–1533, 2013.

[22]F. Pind, A. P. Engsig-Karup, C. H. Jeong, J. S. Hesthaven, M. S. Mejling, and J. Strømann Andersen. Time domain room acoustic simulations using the spectral element method. *J. Acoust. Soc. Am.*, 145(6):3299–3310, 2019.

[23]H. Wang, I. Sihar, R. Pagan Munoz, and M. Hornikx. Room acoustics modelling in the time-domain with the nodal discontinuous Galerkin method. *J. Acoust. Soc. Am.*, 145(4):2650–2663, 2019.

[24]H.-O. Kreiss and J. Oliger. Comparison of accurate methods for the integration of hyperbolic equations. *Tellus*, 24(3):199–215, 1972.

[25]R. Tomiku, T. Otsuru, N. Okamoto, T. Okuzono, and T. Shibata. Finite element sound field analysis in a reverberation room using ensemble averaged surface normal impedance. In *Proc. 40th Int. Cong. Expo. Noise Cont. Eng.*, 2011.

[26]T. Okuzono, N. Shimizu, and K. Sakagami. Predicting absorption characteristics of single-leaf permeable membrane absorbers using finite element method in a time domain. *Appl. Acoust.*, 151:172–182, 2019.

[27]Y. Miki. Acoustical properties of porous materials—modifications of Delany-Bazley models. *J. Acoust. Soc. Jap.*, 11(1):19–24, 1990.

[28]M. A. Biot. The theory of propagation of elastic waves in a fluid-saturated porous solid. I. low frequency range. II. higher frequency range. *J. Acoust. Soc. Am.*, 28:168–191, 1956.

[29]B. Brouard, D. Lafarge, and J. F. Allard. A general method of modeling sound propagation in layered media. *J. Sound Vib.*, 183:129–142, 1995.

[30]H. de Bree, R. Lanoye, S. de Cock, and J. van Heck. In situ, broad band method to determine the normal and oblique reflection coefficient of acoustic materials. In *Proc. Noise. Vib. Conf.*, 2005.

[31]J. Ducourneau, V. Planeau, J. Chatillon, and A. Nejade. Measurement of sound absorption coefficients of flat surfaces in a workshop. *Appl. Acoust.*, 70:710–721, 2009.

[32]A. Richard, E. Fernandez-Grande, J. Brunskog, and C.-H. Jeong. Estimation of surface impedance at oblique incidence based on sparse array processing. *J. Acoust. Soc. Am.*, 141(6):4115–4125, 2017.

[33]C. A. Kennedy and M. H. Carpenter. Additive Runge-Kutta schemes for convection-diffusion-reaction equations. *Appl. Num. Math.*, 44(1):139–181, 2003.

[34]J. S. Hesthaven and T. Warburton. *Nodal Discontinuous Galerkin Methods—Algorithms, Analysis, and Applications*. Springer, New York, 2008. Ch. 3.

[35]A. Taflove and S. C. Hagness. *Computational Electrodynamics: The Finite-Difference Time-Domain Method*. Artech House, Inc., Boston, 3 edition, 2013. Ch. 9.

[36]B. Gustavsen and A. Semlyen. Rational approximation of frequency domain responses by vector fitting. *IEEE Trans. Pow. Del.*, 14(3):1052–1061, 1999.

[37]M. J. Grote, M. K., F. Nataf, and F. Assous. Time-dependent wave splitting and source separation. *J. Comput. Phys.*, 330:981–996, 2017.

[38]D. E. Merewether, R. G. Fisher, and F. W. Smith. On implementing a numeric Huygen's source scheme in a finite difference program to illuminate scattering bodies. *IEEE Trans. on Nucl. Sci.*, 27:1829–1833, 1980.

[39]A. P. Engsig-Karup, S. Glimberg, A. Nielsen, and O. Lindberg. Fast hydrodynamics on heterogeneous many-core hardware. In R. Couturier, editor, *Designing Scientific Applications on GPUs*, pages 251–294. CRC Press / Taylor & Francis Group, Boca Raton, 2013.

[40]S.-I. Thomasson. Reflection of waves from a point source by an impedance boundary. *J. Acoust. Soc. Am.*, 59(4):780–785, 1976.

[41]ISO 354. Acoustics—Measurement of sound absorption in a reverberation room. International organization for standardization, 2003.

[42]M. Ren and F. Jacobsen. A method of measuring the dynamic flow resistance and reactance of porous materials. *Appl. Acoust.*, 39(4):265–276, 1993.

[43]J. S. Suh and P. A. Nelson. Measurement of transient response of rooms and comparison with geometrical acoustic models. *J. Acoust. Soc. Am.*, 105(4):2304–2317, 1999.

[44]R. Kirby. On the modification of Delany and Bazley fomulae. *Appl. Acoust.*, 86:47–49, 2014.

[45]ISO 3382-1. Acoustics—Measurement of room acoustic parameters—Part 1: Performance spaces. International organization for standardization, 2009.